Int. J. Electron. Commun. (AEÜ) 185 (2024) 155452

Contents lists available at ScienceDirect

International Journal of Electronics and Communications

journal homepage: www.elsevier.com/locate/aeue

Regular paper

On-chip coupled-resonator filter with controllable transmission zeros based on hybrid coupling technique

Yanzhu Qi, Yazi Cao *, Bo Yuan, Shichang Chen, Kanglong Zhang, Gaofeng Wang *

MOE Engineering Research Center of Smart Microsensors and Microsystems, School of Electronics and Information, Hangzhou Dianzi University, Hangzhou 310018, China

ARTICLE INFO

Keywords:
Band pass filter (BPF)
Mutual coupling
Transmission zeros (TZs)
Integrated passive device (IPD)

ABSTRACT

A novel on-chip bandpass filter (BPF) design with controllable transmission zeros (TZs) for high out-of-band rejection is proposed using the hybrid coupling technique. The proposed hybrid coupling filter consists of two symmetrical hybrid coupling spiral structures where the mutual electric and magnetic couplings are introduced to generate two TZs in the high frequency band. The center frequency, bandwidth, and transmission zero position of the proposed filter can be well controlled. To illustrate the principle of this configuration, an equivalent circuit with odd- and even-mode analysis is discussed. Moreover, another transmission zero in the low frequency band can be further generated by loading a quasi-distribution structure. The proposed hybrid coupling filter is fabricated using commercial high resistance silicon technology. The measured results show that the proposed filter can achieve a 3 dB bandwidth from 1.85 to 2.33 GHz, which indicates a fractional bandwidth of about 26 %. In addition, more than 40 dB of suppression is achieved from 3.15 to 5.55 GHz. A return loss of 29 dB and a minimum insertion loss of 2.5 dB are achieved at the center frequency with a minimized size 1.6 mm × 0.8 mm. The simulated and measured results are in good agreement.

1. Introduction

Nowadays, mobile phones usually support multiple communication standards (2G/3G/4G/5G), thereby leading to integration of multiple frequency bands in radio-frequency (RF) front-end module (FEM). This integration increases cost, size, and complexity of RF FEM [1,2]. RF filters are a key component of RF FEM, which has a significant impact on performance, size, and other aspects of RF FEM [3,4]. In order to suppress mutual interference between multiple adjacent passbands, the filters with high selectivity, wide suppression, and miniaturization have been the focus of many research endeavors.

Acoustic-wave resonator-based filters (e.g., those exploiting surface-acoustic wave (SAW) and bulk-acoustic-wave (BAW) phenomena) have high Q values and can generate sharp suppression, making them widely used in RF FEM [5]. Its specialized technology limits its application in monolithic microwave integrated circuit (MMIC) and usually can be integrated with other devices through system in package (SiP), which increases the size and complexity of RF FEMs.

Due to merits of multilayer structures, low temperature cofired ceramic (LTCC) has been widely used in designing BPFs [6,7]. LTCC is manufactured by thick film process, which is also difficult to implement in MMIC system. Integrated passive device (IPD) filter based on semiconductor process has merits of small size and easy integration into MMICs. However, its out-of-band suppression has no advantage over the filters based on other processes (LTCC/SAW/BAW). Hence, improving the out-of-band suppression performance of the IPD filters has been widely studied [8–13].

Some designs aimed to achieve excellent out-of-band suppression performance in ultra-wide frequency bands [8–10]. The filter using π-type unit exhibited advantage of ultra-wide stopband due to non-periodic phase of the unit [8]. The low-pass filter cascaded on BPF has been the common method to realize wide stopband [9,10]. In addition, many efforts achieved higher out-of-band suppression by introducing transmission zeros (TZs) [11–15]. Recently, the filters based on coupled resonant structures have been reported [16–23]. This technique can facilitate the miniaturization of filters [16–19] and improve out-of-band suppression by introducing transmission zeros [20–22]. These filters were designed in the millimeter wave band, in which the chip size and wavelength can be comparable and thus more suitable to use distributed structure design. In [23], the filter designed with differential

* Corresponding authors.
E-mail addresses: caoyazi@hdu.edu.cn (Y. Cao), gaofeng@hdu.edu.cn (G. Wang).

https://doi.org/10.1016/j.aeue.2024.155452
Received 12 May 2024; Accepted 19 July 2024
Available online 21 July 2024
1434-8411/

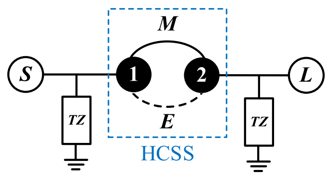

Fig. 1. Topology of the proposed coupled resonator filter with hybrid coupling technique.

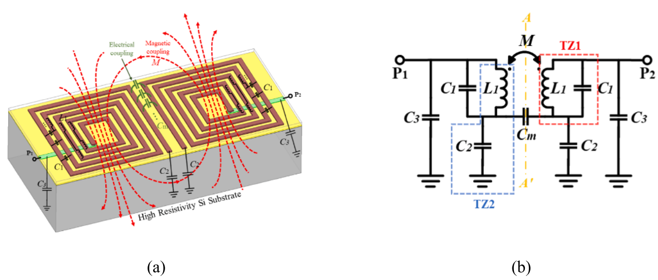

Fig. 2. Hybrid coupling spiral structure: (a) Layout view. (b) Equivalent circuit model.

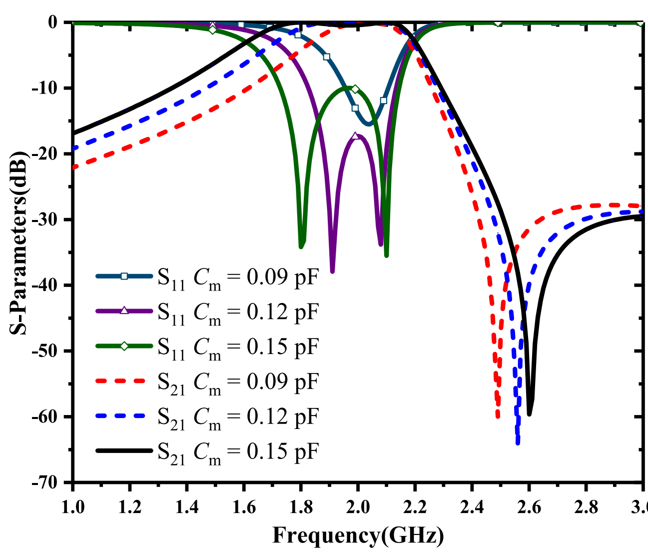

Fig. 3. Circuit simulated S-parameters of the hybrid coupling spiral structure, while C_m is swept from 0.09 to 0.15 pF, with $L_1 = 14$ nH, M=1.2 nH, $C_1 = 0.13$ pF, $C_2 = 0.23$ pF and $C_3 = 0.1$ pF.

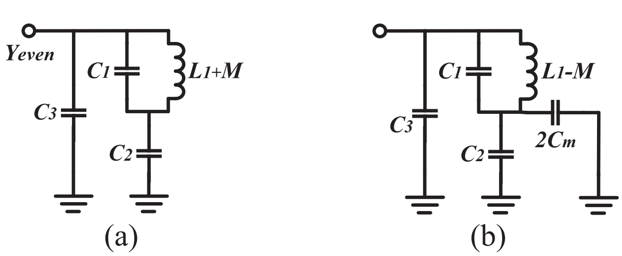

Fig. 4. Equivalent circuit models of hybrid coupling spiral structure: (a) Even-mode excitation. (b) Odd-mode excitation.

transformer structures in sub-6 GHz achieved very compact size and high rejection, but its design structure was special and not universal.

In this work, a novel on-chip BPF design with controllable TZs for high out-of-band rejection is proposed using hybrid coupling technique. By investigating the mutual electric and magnetic couplings, the proposed hybrid coupling filter can generate two TZs in the high frequency band. An equivalent circuit of the designed hybrid coupling spiral structures is constructed to illustrate the principle of this technique. In addition, a quasi-distribution structure is proposed to generate one extra TZ in the low frequency band. Using theoretical analysis for the hybrid coupling along with circuit and EM simulations, the transmission zeros can be well controlled. Finally, a sub-6 GHz hybrid coupling filter is designed and fabricated using the high resistance silicon (HRS) technology. The measured results show that the proposed filter has a 3-dB bandwidth of 26 % from 1.85 to 2.33 GHz, approximately. The minimum insertion loss is 2.5 dB. A harmonic suppression more than 40 dB is achieved from 3.15 to 5.55 GHz. The filter chip area is only 1.6 mm × 0.8 mm (0.038 × 0.019λ_g^2). The designed hybrid coupling BPF has achieved a competitive performance by comparison to the state-of-the-art works.

2. Hybrid coupling technique

Fig. 1 illustrates topology of the proposed hybrid coupling filter. In the proposed hybrid coupling spiral structure (HCSS), two resonators 1 and 2 are electrically (E) and magnetically (M) coupled, while the other two nonresonant nodes are utilized as the source (S) and load (L) for input and output, respectively. In addition, two identical transmission zero (TZ) circuits are added between S and 1 and between 2 and L, respectively, thereby introducing an additional TZ in the low frequency end.

2.1. Hybrid coupling spiral structure

Spiral inductors can be used in on-chip filter designs since spiral inductors self-resonate at high frequencies due to the parasitic capacitance between the structures. The resonance unit of the filter can be constructed by shorting one end of the spiral inductor to ground through a series capacitor. The layout view and equivalent circuit of the proposed hybrid coupling BPF are shown in Fig. 2.

To illustrate the operational principle of the structure in Fig. 2(a), a simplified equivalent circuit model that represents its behavior is given in Fig. 2(b). The main structure consists of two spiral resonators placed symmetrically. C_1 and L_1 denote the self-capacitance and self-inductance of the spiral resonator, respectively. C_2 is the capacitive coupling between the end of the spiral resonator and the ground. C_3 is the bypass capacitance between the feeding line and the ground. To miniaturize the design, it is best to keep the values of L_1 and C_1 unchanged because these two parameters are determined by the physical size of the spiral resonator structure. The loaded capacitor C_2 can be used to control the resonant frequency without adding much extra area since the physical size of the capacitor is much smaller than that of the spiral resonator structure. Furthermore, since MIM capacitors are often available in silicon-based technologies, adjusting the capacitance value becomes a better option for tuning the resonant frequency.

Consider the coupling between two resonators. The magnetic and electrical couplings are denoted as M and C_m, respectively. By tuning the values of M and C_m, the bandwidth of the BPF, which is related to the coupling coefficient, can be adjusted. The mixed coupling coefficient k_X between every two adjacent resonators can be represented by [24]:

$$k_X \approx ke + km = \frac{Cm}{C2} + \frac{M}{L1}$$

where k_e and k_m are the electrical and magnetic coupling coefficients respectively. Since the two resonant elements of the filter are symmetric, the coupling coefficient k can be written by applying synchronous tuning:

$$k_X = \pm \frac{f_{r2}^2 - f_{r1}^2}{f_{r2}^2 + f_{r1}^2}$$

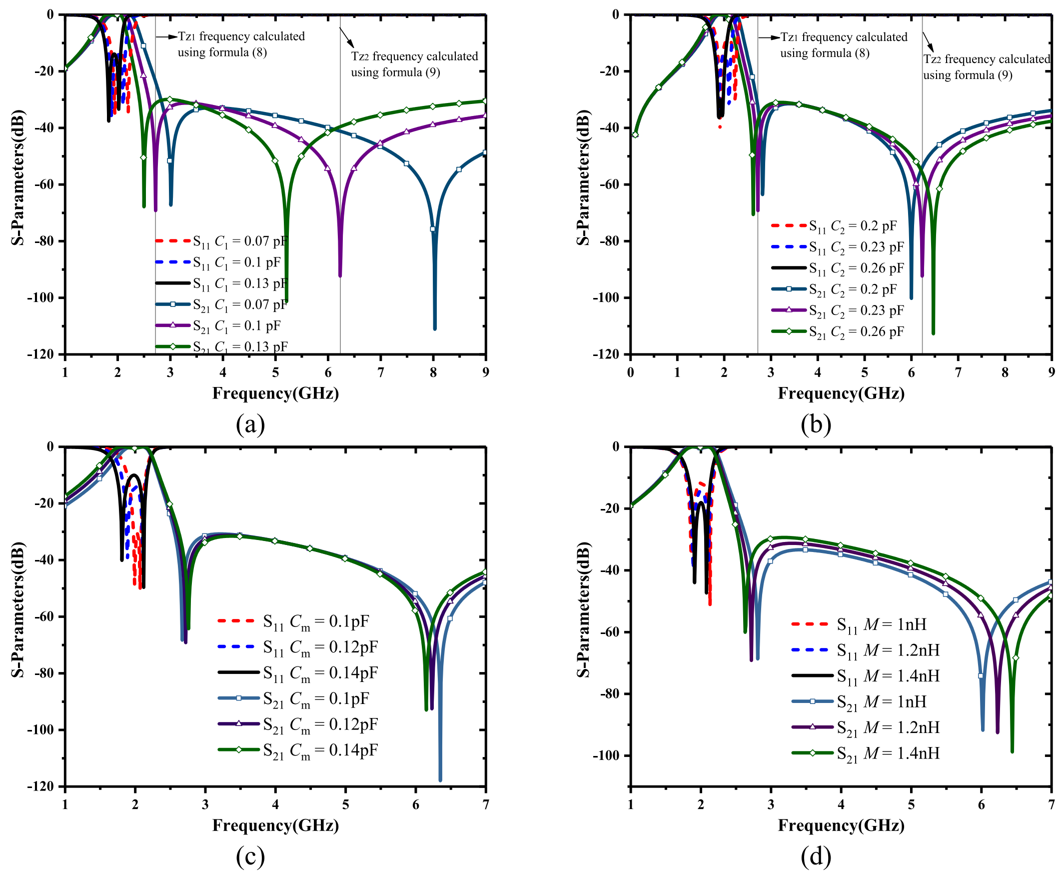

Fig. 5. Circuit simulated S parameters of the hybrid coupling spiral structure. (a) C_1 is swept from 0.07 to 0.13 pF. (b) C_2 is swept from 0.2 to 0.26 pF. (c) Cm is swept from 0.1 to 0.14 pF. (d) M is swept from 1 to 1.4 nH. (Default value: L_1 = 15 nH, M=1.2 nH, C_1 = 0.1 pF, C_2 = 0.23 pF, C_m = 0.12 pF and C_3 = 0.1 pF).

where f_{r1} and f_{r2} represent the two resonant frequencies when two resonators are coupled with each other. To understand the effects of electrical and magnetic couplings on the transmission pole (TP) distribution, Fig. 3 shows the frequency responses of TPs with different values of C_m. With increasing C_m, the two TPs gradually become farther away, and thus the bandwidth increases.

The even- and odd-mode analysis method is applied here due to the symmetrical topology arrangement. Fig. 4(a) and (b) show the even- and odd-mode circuits of Fig. 2, respectively. The admittances of the even- and odd-mode transmission lines can be denoted as Y_{even} and Y_{odd}, respectively. The circuit can then be modeled as a reciprocal two-port network by its admittance matrix [Y], which can be written as [25]:

$$[Y] = \begin{pmatrix} \dfrac{Y_{even}+Y_{odd}}{2} & \dfrac{Y_{even}-Y_{odd}}{2} \\ \dfrac{Y_{even}-Y_{odd}}{2} & \dfrac{Y_{even}+Y_{odd}}{2} \end{pmatrix}$$

where Y_{even} and Y_{odd} are, respectively, the even- and odd-mode input admittances:

$$Y_{even} = \frac{j\omega C_2 - j\omega^3(L_1+M)C_1C_2}{1-\omega^2(L_1+M)C_1-\omega^2(L_1+M)C_2} + j\omega C_3$$

$$Y_{odd} = \frac{j\omega(C_2+2C_m) - j\omega^3(L_1-M)C_1(C_2+2C_m)}{1-\omega^2(L_1-M)C_1-\omega^2(L_1-M)(C_2+2C_m)} + j\omega C_3$$

Then the scattering parameters of the two-port network can be expressed as [26]:

$$S_{21} = \frac{Y_0(Y_{even}-Y_{odd})}{(Y_0+Y_{even})(Y_0+Y_{odd})}$$

where Y_o is the load admittance. For the proposed resonator with two tapped ports, it is possible to find the transmission zero by solving $Y_{even} - Y_{odd} = 0$.The formula of the generated TZ can be found as follows:

$$\omega_{Tz0} = 0$$

$$\omega_{Tz1} = \sqrt{\frac{2(P+Q)}{2L_3L_2C_1(C_2-C_M)}}/2C_1$$

$$\omega_{Tz2} = \sqrt{\frac{2(-P+Q)}{2L_3L_2C_1(C_2-C_M)}}/2C_1$$

Where:

$$P = \sqrt{\frac{(A+D-E)}{L_3^2} - \frac{2A}{L_2L_3} + \frac{(A-D+E)}{L_2^2}}$$

$$Q = G\left(\frac{1}{L_2C_M} + \frac{1}{L_3C_M} - \frac{1}{L_2C_2} - \frac{1}{L_3C_2} - \frac{1}{L_2C_1} + \frac{1}{L_3C_1}\right)$$

$$A = C_1^2C_2^2L_3^2L_2^2 - 2C_1^2C_2C_ML_3^2L_2^2 + C_1^2C_M^2L_3^2L_2^2 + C_2^2C_M^2L_3^2L_2^2$$

$$D = 2C_1C_2^2C_ML_3^2L_2^2$$

$$E = 2C_1C_2C_M^2L_3^2L_2^2$$

$$G = C_1C_2L_3L_2C_M$$

$$L_2 = L_1 - M, L_3 = L_1 + M, C_M = C_2 + 2C_m$$

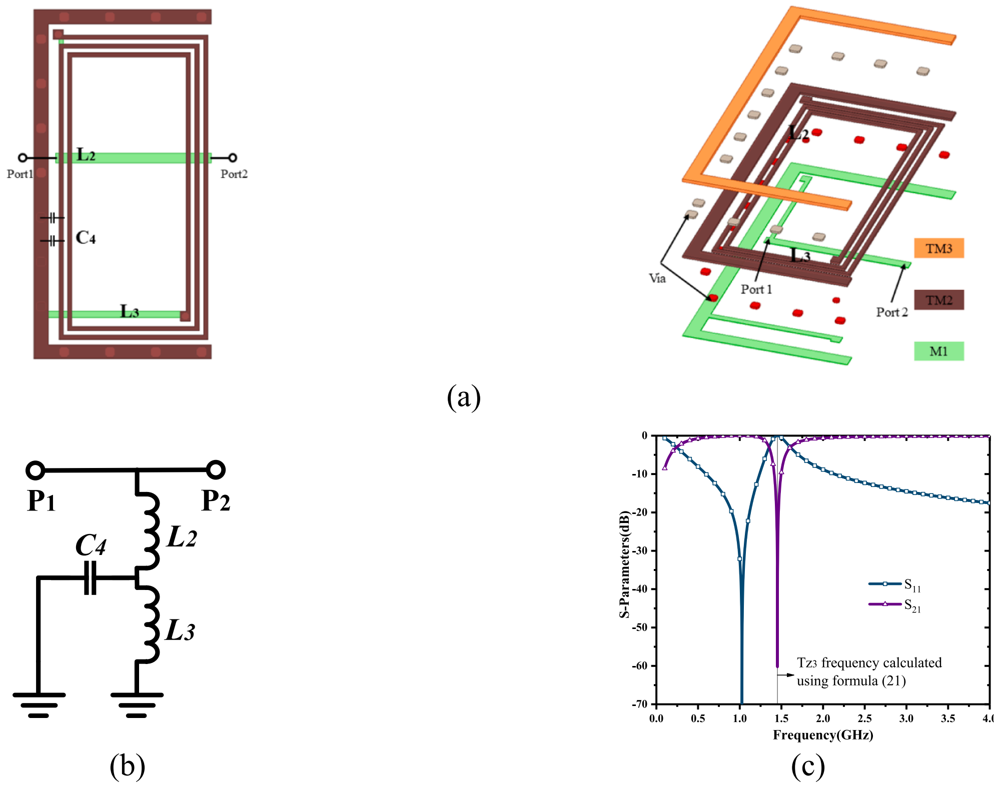

Fig. 6. Quasi-distribution structure for additional TZ. (a) Layout view. (b) Equivalent circuit models. (c) Circuit simulation result (where $L_2 = 8$ nH, $L_3 = 8$ nH and $C_4 = 3$ pF).

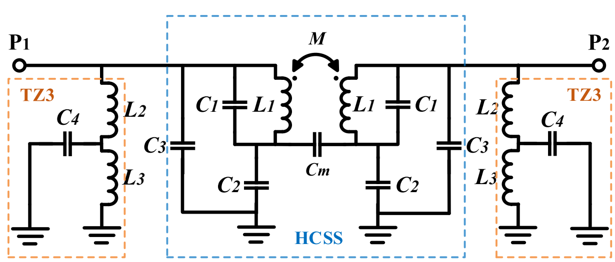

Fig. 7. Equivalent circuit model of the proposed filter.

Without considering the case of $\omega = 0$, it is clearly seen from (7)–(9) that the presented circuit model can produce two TZs. As shown in the equivalent circuit in Fig. 2(b), the two high-frequency transmission zeros TZ_1 and TZ_2 are generated by the hybrid coupling spiral structure. The inductors L_1 and C_1 form a parallel resonant circuit and produce a transmission zero TZ1. L_1 and C_2 form a series resonant circuit and produce transmission zero TZ2. Other devices such as C_m and M affect the transmission zero by affecting the values of C_2 and L_1, respectively. However, it is difficult to directly see the impact on the BPF transfer function due to variations of different circuit elements. Thus, circuit simulation is employed to assist the analysis so that the insight of this design can be further explored. Circuit simulated S parameters of the proposed BPF with different values for C_1, C_2, C_m and M are plotted in Fig. 5.

As shown in the high-frequency range of Fig. 5(a), with increasing capacitor C_1, both the two TZs move to lower frequencies, and the TZ at the higher frequency is more affected. As shown in the high-frequency range of Fig. 5(b), with increasing capacitor C_2, the TZ at the lower frequency moves to an even lower frequency, whereas the TZ at the higher frequency moves to an even higher frequency. Therefore, by adjusting the values of C_1 and C_2, one can readily adjust the position of

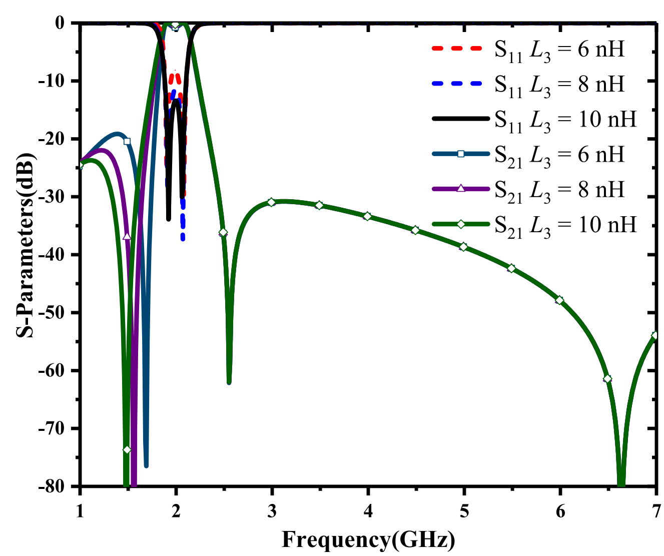

Fig. 8. EM simulated S_{21} of the BPF, while L_3 is swept from 6 to 10 nH, $L_2 = 8$ nH, and $C_4 = 3$ pF.

the filter's two high-frequency TZs. In addition, inductor L_1 can also be utilized to adjust TZs and passband of the filter. But it may significantly affect the chip area. Therefore, it is best to first determine the inductance value according to the given chip area, and then carefully optimize the frequency response of the BPF by adjusting values of the capacitors. C_m and M mainly control the bandwidth of the filter and the position of the transmission zero, as shown in Fig. 5(c) and (d). The relationship between the bandwidth of the filter and C_m and M is obtained by circuit simulation and considering the position of the transmission zero, the

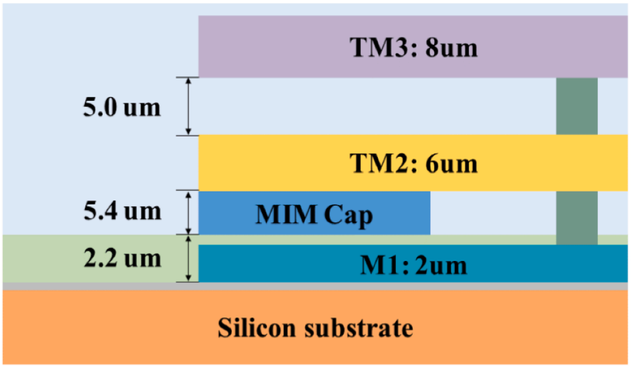

Fig. 9. Metal stack-up of the high resistance silicon technology.

expected filter response is obtained by optimizing the values of C_m and *M*.

2.2. Quasi-distribution structure

Although the hybrid coupling spiral structure improves stopband rejection and selectivity with two TZs in the high frequency band, the stopband rejection is poor in the low frequency band. Therefore, as shown in Fig. 6(a), a new independent quasi-distribution structure for additional TZ is proposed to enhance the out-of-band suppression in the low frequency band. This structure is mainly composed of a rectangular spiral inductor, in which one end serves as the input/output, while the other end is grounded. The structure is surrounded by a ring of ground, so there is a distributed capacitance to the ground.

The equivalent circuit of the structure is given in Fig. 6(b). The circuit can then be modeled as a two-port network by an admittance matrix [Y], which can be written as follows:

$$Y = \left(\frac{1}{j\omega L_3} + j\omega C_4\right) // \frac{1}{j\omega L_2}$$

The scattering parameter can be obtained as [24]:

$$S_{21} = \frac{2}{2 + YZ_0}$$

From (17) and (18), the scattering parameter can be derived as

$$S_{21} = \frac{2j\omega(L_2 + L_3) - 2j\omega^3 L_2 L_3 C_4}{2j\omega(L_2 + L_3) - 2j\omega^3 L_2 L_3 C_4 + Z_0(1 - \omega^2 L_3 C_4)}$$

By forcing $S21 = 0$, TZs can be obtained at the following frequencies:

Table 1
Physical dimensions of the BPF.

w_1	w_2	w_3	w_4	s_1	s_2	s_3	s_4	s_5
11	23	10	33	11	10	18	13	25.5
s_6	s_7	d_1	d_2	d_3	d_4	d_5	d_6	Unit: μm
11.5	24	95	171	260	617	800	1600	

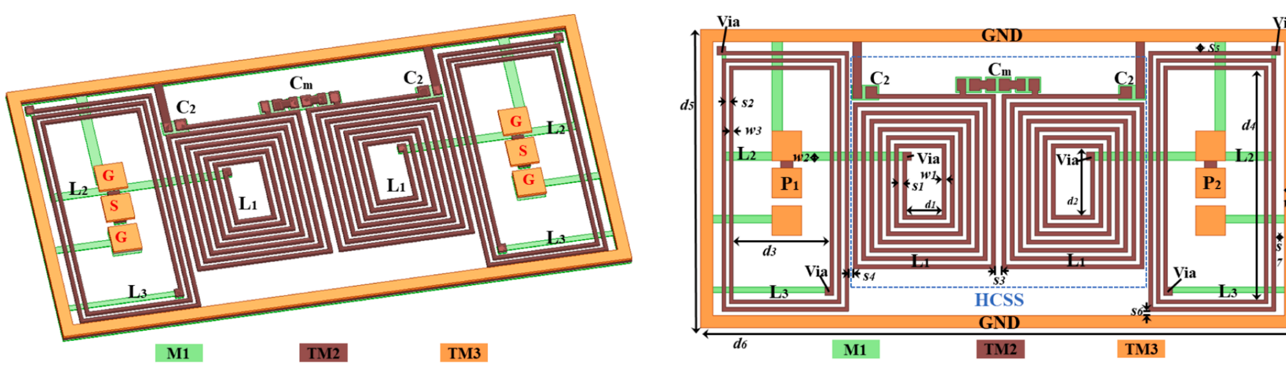

(a) (b)

Fig. 10. The proposed hybrid coupling filter. (a) 3-D view. (b) 2-D view.

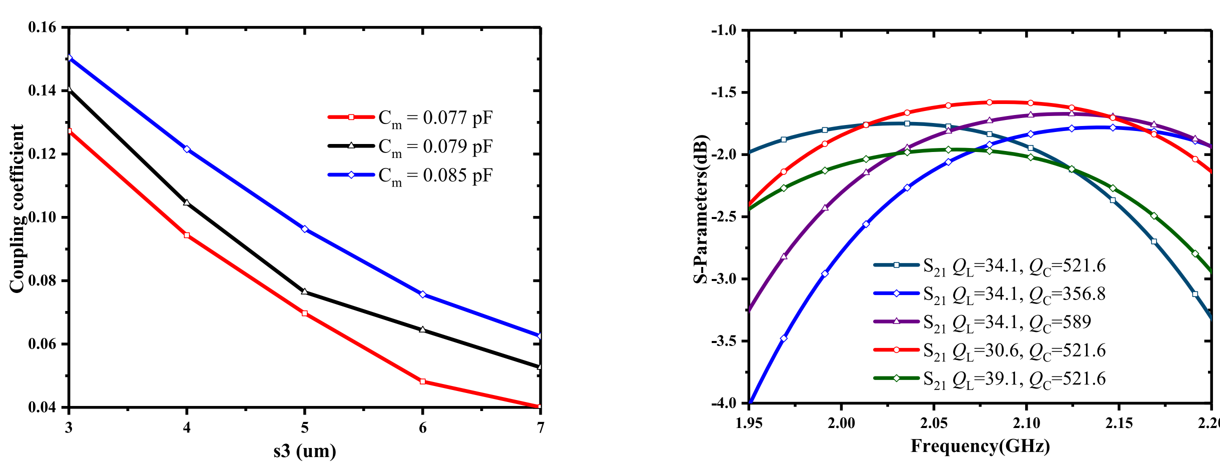

(a) (b)

Fig. 11. (a) Effect of distance $s3$ and C_m on coupling coefficient. (b) Impact of Q_C and Q_L on S_{21}.

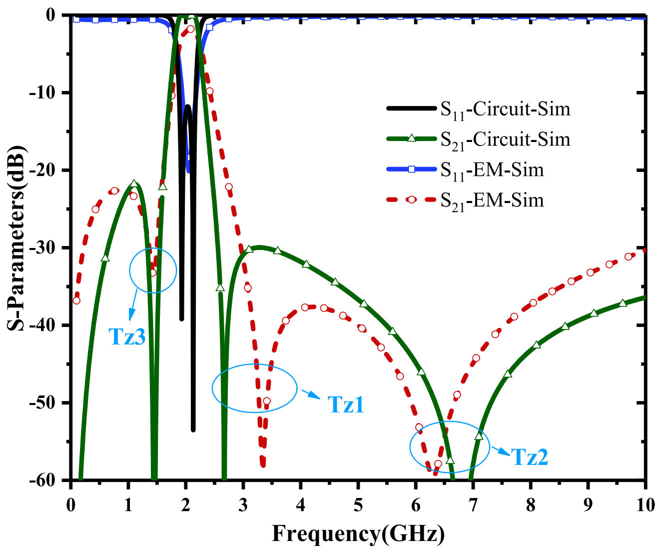

Fig. 12. S-parameters of EM simulation and equivalent circuit model (where $L_1 = 14$ nH, $L_2 = 8$ nH, $L_3 = 8$ nH, M=1.2 nH, $C_m = 0.085$ pF, $C_1 = 0.1$ pF, $C_2 = 0.23$ pF, $C_3 = 0.1$ pF, and $C_4 = 3$ pF).

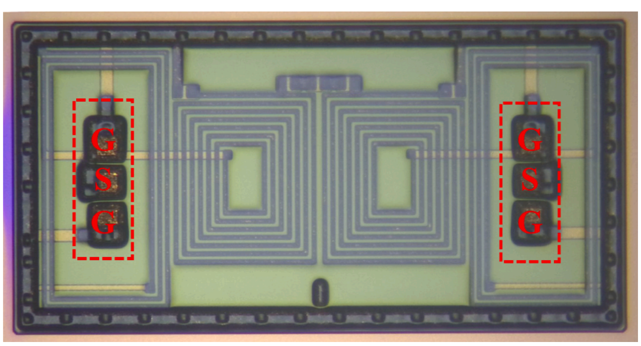

Fig. 13. Die photograph of the proposed hybrid coupling filter.

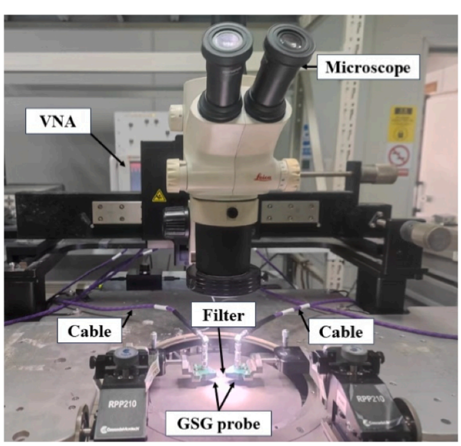

Fig. 14. Test instrument photograph.

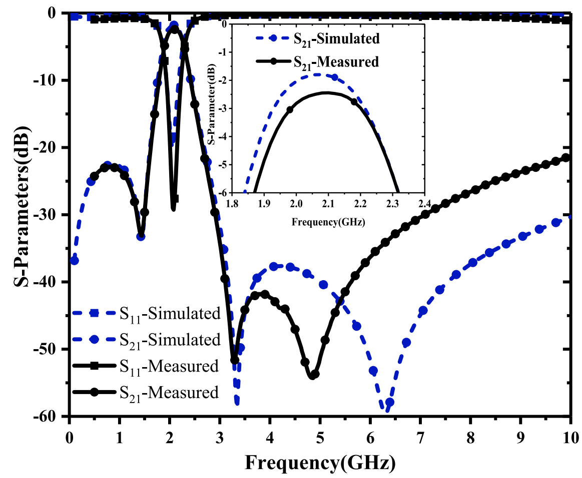

Fig. 15. Comparisons between the EM-simulated and measured results.

$$\omega_{tz0} = 0$$

$$\omega_{tz1} = \sqrt{\frac{L_2 + L_3}{L_2 L_3 C_4}}$$

Transmission zero TZ3 is generated by L_2, L_3 and C_4. C_4 form series resonant circuit with L_2 and parallel resonant circuit with L_3 respectively. As deduced from (21), by changing the values of L_2, L_3, or C_4, the resonance frequency can be effectively controlled. The simulated S-parameter response of the TZ circuit is shown in Fig. 6(c).

2.3. Proposed filter

According to Fig. 1, the hybrid coupling spiral structure and the quasi-distribution structure are combined together to construct the proposed hybrid coupling filter. The complete equivalent circuit of the proposed hybrid coupling filter is shown in Fig. 7. The circuit simulations of the equivalent circuit are performed and depicted in Fig. 8. The TZ position in the lower stopband can be adjusted about from 1.5 to 1.7 GHz by changing the L_3 value, which does not virtually have much impact on the passband frequency and the upper stopband TZs.

3. Design

A high resistance silicon technology is herein used in the design, which provides one metal layer M1 of aluminum and two thick metal layers TM2 and TM3 of copper on top. The additional metal–insulator–metal (MIM) layer is placed between M1 and TM2. A cross-section view of the metal stack-up is given in Fig. 9. The height of the silicon substrate is 250 μm. The relative dielectric constant of silicon substrate is 11.7, and the dielectric loss tangent is 0.003.

As shown in Fig. 10, the design uses the middle metal layer TM2 to realize the main spiral structure, and the lower layer M1 to lead the cross-layer. It is worth noting that although the thickness of the TM3 layer is thicker, because the line spacing of the TM2 layer (10 μm) is smaller than that of the TM3 layer (15 μm), considering the miniaturization of the filter, the TM2 layer is used to achieve the main spiral structure. If the filter is expected to have a smaller loss without concern for size, a thicker TM3 layer can also be used to achieve the main spiral structure, which is a trade-off between size and insertion loss. A 3-D view and 2-D view of the proposed filter is shown in Fig. 10. Load capacitor C_2 is implemented with MIM capacitor for easy control of frequency response. Limited by the minimum line spacing of the process, it is difficult to achieve the required capacitance value only by the edge coupling between the two spiral structures. Therefore, an additional MIM capacitor C_m is added to enhance the coupling. The

Table 2
Performance comparisons between this paper and other works.

Ref.	f_c (GHz)	IL (dB)	3-dB FBW (%)	TZ	Area (λ_g^2)	Rejection /Stopband	Order of BPF	Technology
[2]-2	3	1.5	131	1	0.097 × 0.032	47 dB/10 f_0	5	GaAs IPD
[3]-1	23	3.8	16.7	1	N/A	30 dB/2.91 f_0	2	0.13-μm SiGe
[4]	2.6	2.47	10.2	2	0.042 × 0.035	28 dB/4.15 f_0	2	LTCC
[7]	5.54	2.04	22	2	0.133 × 0.08	16.44 dB/–	3	GaAs IPD
[8]-A1	3.36	2.61	19.3	2	0.1 × 0.05	N/A	5	GaAs IPD
[11]	3.58	1.45	73.92	3	0.044 × 0.022	20 dB/26.5 f_0	5	GaAs IPD
[13]-2	14	2.5	28.6	2	N/A	30 dB/1.86 f_0	2	0.13-μm SiGe
[15]	12.25	3.42	40.8	2	0.186 × 0.098	20 dB/3.265 f_0	2	AME solution
[16]	33	1	59	2	0.074 × 0.09	20 dB/2.47 f_0	2	0.1-μm GaAs
[17]	2.5	0.9	112	3	0.034 × 0.021	25 dB/8.8 f_0	5	GaAs IPD
[18]	3.75	1.5	24	5	0.046 × 0.031	20 dB/8.3 f_0	2	HRS
This work	**2.065**	**2.5**	**26**	**3**	**0.038 × 0.019**	**30 dB/3.53 f_0**	**2**	**HRS**

electromagnetic hybrid coupling between the two spiral structures can be adjusted by spacing $s3$ and value of C_m, the influence of the value of capacitance C_m and the distance $s3$ on the coupling coefficient is shown in Fig. 11(a). The influence of the Q value of inductor (Q_L) and capacitor (Q_C) on the insertion loss is shown in Fig. 11 (b). Different Q_L and Q_C will cause the filter frequency to shift slightly. The Q value of inductor is small and has a more significant influence on the insertion loss of the filter. The hybrid coupling spiral structure and the quasi-distribution structure are connected in series and surrounded by a ground ring, while the ground ring is realized by stacking all metal layers together. Different width of the ground ring will slightly affect the frequency of the filter, basically do not affect the overall response of the filter.

A 2-D view of the proposed filter is shown in Fig. 10(b). Key dimensions are marked in the Fig. 10(b), and the corresponding values are shown in Table 1. In order to validate the circuit analysis in the preceding section, the results of the equivalent circuit model (see Fig. 7) are compared with those of the full-wave electromagnetic (EM) simulation using UltraEM [27], as shown in Fig. 12. A reasonable agreement has been obtained between the two results, and the related resonant frequency and transmission zero point are basically consistent. Because the equivalent circuit model uses the ideal capacitor and inductor devices, and does not consider the resistance of the device itself and the coupling between the devices. Device and interconnect resistance losses cause the filter's sideband attenuation to be less steep than that of an ideal filter circuit model and the coupling between devices will cause the shift of transmission zero and passband.

4. Fabrication and measurement

To evaluate the performance of the proposed hybrid coupling filter, the prototype is fabricated using the high resistance silicon technology. The chip photo is shown in Fig. 13. Including the pads, the full size of the chip is only 1.6 × 0.8 mm^2. This BPF is measured and the S-parameters of the BPFs are measured up to 45 GHz. This measurement setup includes Keysight Technologies Inc.'s vector network analyzer (VNA) PNA-X N5247A, Cascade Microtech Summit 11,000 probe station, and a pair of cables and GSG probes with a spacing of 100 μm, as shown in the Fig. 14. Before the measurement, use a commercial calibration substrate to perform short-open-load-thru (SOLT) calibration on the two ports to minimize the adverse effects of cables, probes, and VNA. After the calibration, the GSG probe is connected to the GSG pad of the filter to be tested through the probe station, and the filter chip is connected to the instrument VNA for testing.

Both the measured and EM simulated S parameters of the proposed hybrid coupling filter are plotted in Fig. 15. The measured center frequency appears at 2.065 GHz, in which the measured minimum in-band insertion loss of the filter is 2.5 dB. In order to achieve a narrower bandwidth of the two passbands, the two poles in the passbands are merged into one pole by adjusting the coupling. The simulation results show that the proposed filter can achieve a good the insertion loss, but due to the manufacturing tolerance and the loss tangent parameters in the actual processing, the measured insertion loss performance deteriorates. A 3-dB bandwidth is achieved from 1.85 to 2.33 GHz, which indicates a fractional bandwidth (FBW) of 26 %. One can observe a reasonably good agreement between the EM-simulated and measured results in terms of the in-band frequency responses. The frequency deviation of the measured and simulated results of TZ1 is mainly caused by fabrication tolerance between the sides of the spiral line, the self-capacitance C_1 is inconsistent with that of the simulation structure. In addition, the longer transmission line length further amplifies this deviation and shifts the frequency of transmission zero. According to the measured results, the harmonics are suppressed by more than 40 dB from 3.15 to 5.55 GHz and more than 30 dB from 2.92 to 7.3 GHz due to the two transmission zeros generated in the stopband.

For comparison purposes, the performance comparisons between this work and some other state-of-the-art designs are illustrated in Table 2. Specifically, the proposed filter is more compact. When compared to the similar designs given in [2,3,8,11,15,17], and [18], the proposed BPF achieves lower insertion loss or higher selectivity. By comparison to the BPF designs given in [13] and [16], the proposed filter achieves wider stopband or higher out-of-band rejection. Since different filters are designed for different specifications, it is difficult to provide an apple-to-apple comparison. As can be seen, the presented design demonstrates a good tradeoff between compactness, selectivity, and minimum in-band insertion-loss level.

5. Conclusion

A novel on-chip bandpass filter design with controllable transmission zeros for high out-of-band rejection has been introduced by virtue of a hybrid coupling technique. This BPF consists of hybrid coupling spiral structure and quasi-distribution structure. The hybrid coupling spiral structure can generate two high-frequency TZs, whereas the quasi-distribution structure contributes an additional TZ at the low frequency. In order to illustrate the working principle, equivalent circuit models of resonators and BPF have been constructed to study their transmission characteristics. The bandwidth, center frequency and TZs of the BPF can be flexibly controlled by readily adjusting the corresponding element or coupling coefficient in the equivalent circuit model. The BPF has been implemented and fabricated using a high resistance silicon technology. Good agreement between the simulated and measured results can be observed. The proposed BPF can achieve a 3 dB bandwidth from 1.85 to 2.33 GHz which indicates a fractional bandwidth of less than 26 %. In addition, more than 40 dB suppression is achieved from 3.15 to 5.6 GHz. Furthermore, a return loss of 29 dB and a minimum insertion loss of 2.5 dB can be achieved at the center frequency of 2.065 GHz. The fabricated filter size is only 1.6 mm × 0.8 mm (0.038 × 0.019λ_g^2). Based on the overall performance, the proposed BPF is promising and attractive for the design of high suppression RF integrated circuits.

CRediT authorship contribution statement

Yanzhu Qi: Writing – original draft. **Yazi Cao:** Writing – review & editing, Writing – original draft. **Bo Yuan:** Writing – review & editing. **Shichang Chen:** Writing – review & editing. **Kanglong Zhang:** Writing – review & editing. **Gaofeng Wang:** Writing – review & editing.

Declaration of competing interest

The authors declare that they have no known competing financial interests or personal relationships that could have appeared to influence the work reported in this paper.

Data availability

No data was used for the research described in the article.

Acknowledgement

This work was supported by the National Natural Science Foundation of China of China under Grants 92373202, 62141409, Zhejiang Provincial Natural Science Foundation under Grant No. LQ24F010010, National Key Research and Development Program of China under Grant 2019YFB2205003, and Zhejiang Provincial Key Research & Development Project under Grant 2021C01041.

References

[1] Kim T, Lee D, Kwon K. CMOS channel-selection low-noise amplifier with high-Q RF band-pass/band-rejection filter for highly integrated RF front-ends. IEEE Microw Wireless Compon Lett 2020;30(3):280–3. https://doi.org/10.1109/LMWC.2020.2966361.
[2] Mani DS, Inabathini SR. A systematic approach for the development of wide band band pass filters using resonators. AEU - Int J Electr Commun 2024;175:155115. https://doi.org/10.1016/j.aeue.2023.155115.
[3] Sun F, Zhu H, Zhu X, Yang Y, Gómez-García R. Design of on-chip millimeter-wave bandpass filters using multilayer patterned-ground element in 0.13-μm (Bi)-CMOS technology. IEEE Trans Microw Theory Technol 2019;67(12):5159–70. https://doi.org/10.1109/TMTT.2019.2949293.
[4] Torabi Y, Farahani MTH, Dadashzadeh G, Lalbakhsh A. A wide bandstop filter using negative permeability achieved by complementary electrical L-C resonators. AEU - Int J Electr Commun 2024;177:155190. https://doi.org/10.1016/j.aeue.2024.155190.
[5] Liu B-G, Zhou Y-J, Cheng C-H. Miniaturized ultra-wideband bandpass filter with ultra-wide stopband using π-type unit with inductive loading on integrated passive device. IEEE Trans Circuits Syst II, Exp Briefs 2021;68(11):3406–10. https://doi.org/10.1109/TCSII.2021.3078154.
[6] Xu J-X, Zhang XY, Zhao X-L, Xue Q. Synthesis and implementation of LTCC bandpass filter with harmonic suppression. IEEE Trans Compon, Packag, Manuf Technol 2016;6(4):596–604. https://doi.org/10.1109/TCPMT.2016.2531180.
[7] Yang Y, Yongle Wu, Wang W. IPD bandpass filter chip based on the filter prototype realized by new compact resonators. AEU - Int J Electr Commun 2022;144:154055. https://doi.org/10.1016/j.aeue.2021.154055.
[8] Liu B-G, Zhou Y-J, Cheng C-H. Miniaturized ultra-wideband bandpass filter with ultra-wide stopband using π-type unit with inductive loading on integrated passive device. IEEE Trans Circuits Syst II, Exp Briefs 2021;67(11):3406–10. https://doi.org/10.1109/TCSII.2021.3078154.
[9] Jiang Y, Feng L, Zhu H, Feng W, Chen H, Shi Y, et al. Bandpass filter with ultra-wide upper stopband on GaAs IPD technology. IEEE Trans Circuits Syst II, Exp Briefs 2022;69(2):389–93. https://doi.org/10.1109/TCSII.2021.3096936.
[10] Luo X-H, Cheng X, Zhang L, Chen F-J, Xia X-L, Han J-A, et al. A miniaturized on-chip BPF with ultrawide stopband based on lumped Pi-section and source-load coupling. IEEE Microw Wireless Compon Lett 2019;29(8):516–9. https://doi.org/10.1109/LMWC.2019.2924088.
[11] Xu Y, Wu Y, Wu H, Yang Y, Wang W. Wideband high selectivity filter chips with adjustable bandwidth based on IPD technology. IEEE Trans Circuits Syst II, Exp Briefs 2022;69(11):4273–7. https://doi.org/10.1109/TCSII.2022.3186182.
[12] Shi Y, Zhou P, Feng W, Shen Y, Tang W. A GaAs-based ultra-wideband common-mode filter chip with four transmission zeros and equalization integration. IEEE Trans Electromagn Compat 2020;62(5):2002–11. https://doi.org/10.1109/TEMC.2019.2943508.
[13] Zhu H-R, Wang W-T. High selectivity millimeter-wave on-chip band-pass filter with semi-lumped dual-mode resonator by using GaAs technology. IEEE Electron Device Lett 2023;44(5):729–32. https://doi.org/10.1109/LED.2023.3254459.
[14] Zheng Y, Tian H, Dong Y. Design of compact GaAs-based on-chip filter and duplexer with high selectivity and wide stopband. IEEE Microw Wireless Tech Lett 2024;34(1):33–6. https://doi.org/10.1109/LMWT.2023.3335114.
[15] Elsaidy E, Barakat A, Abdel-Rahman AB, Allam A, Pokharel RK. Ultracompact CMOS 60-GHz tapped-line combline BPF with two transmission zeros using defected ground structures. IEEE Trans Compon, Packag, Manuf Technol 2018;8(9):1642–9. https://doi.org/10.1109/TCPMT.2018.2861411.
[16] Zhu H, Zhu X, Yang Y, Sun Y. Design of miniaturized on-chip bandpass filters using inverting-coupled inductors in (Bi)-CMOS technology. IEEE Trans Circuits Syst i, Reg Papers 2020;67(2):647–57. https://doi.org/10.1109/TCSI.2019.2948754.
[17] Xiaotong Xu, Zhu H, Feng W, Shen G, Che W, Xue Q. A miniaturized low-loss absorptive bandpass filter using IPD technology. AEU - Int J Electr Commun 2024;177:155234. https://doi.org/10.1016/j.aeue.2024.155234.
[18] Zhang J, Xu J-X, Yao C, Zhang XY. Miniaturized high-selectivity high-resistivity-silicon IPD bandpass filter based on multiple transmission paths. IEEE Electron Device Lett 2024;45(4):534–7. https://doi.org/10.1109/LED.2024.3364692.
[19] Yang Y, Zhu X, Xue Q. Design of an ultracompact on-chip bandpass filter using mutual coupling technique. IEEE Trans Electron Devices 2018;65(3):1087–93. https://doi.org/10.1109/TED.2018.2797304.
[20] Yang Y, Zhu X, Dutkiewicz E, Xue Q. Design of a miniaturized on-chip bandpass filter using edge-coupled resonators for millimeter-wave applications. IEEE Trans Electron Devices 2017;64(9):3822–8. https://doi.org/10.1109/TED.2017.2720185.
[21] Li M, Yang Y, Xu KD, Zhu X, Wong SW. Microwave on-chip bandpass filter based on hybrid coupling technique. IEEE Trans Electron Devices 2018;65(12):5453–9. https://doi.org/10.1109/TED.2018.2876324.
[22] Liu Y, Xu K-D. Millimeter-wave bandpass filters using on-chip dual-mode resonators in 0.13-μm SiGe BiCMOS technology. IEEE Trans Microw Theory Technol 2023;71(8):3650–60. https://doi.org/10.1109/TMTT.2023.3242317.
[23] Li Y, Wang C, Kim N-Y. Design of very compact bandpass filters based on differential transformers. IEEE Microw Wireless Compon Lett 2015;25(7):439–41. https://doi.org/10.1109/LMWC.2015.2427660.
[24] Hong J-S, Lancaster MJ. Microstrip filters for RF/microwave applications. New York: John Wiley & Sons; 2001. p. 245–51.
[25] Zhu H, Yang Y, Zhu X, Sun Y, Wong S-W. Miniaturized resonator and bandpass filter for silicon-based monolithic microwave and millimeter-wave integrated circuits. IEEE Trans Circuits Syst i, Reg Papers 2018;65(12):4062–71. https://doi.org/10.1109/TCSI.2018.2839701.
[26] Sun S, Shi J, Zhu L, Rustagi SC, Mouthaan K. Millimeter-wave bandpass filters by standard 0.18-μm CMOS technology. IEEE Electron Device Lett 2007;28(3):220–2. https://doi.org/10.1109/LED.2007.891305.
[27] UltraEM V202209, Faraday Dynamics, Inc., Hangzhou, Zhejiang, China, 2022.